Received: 5 December 2019 | Revised: 8 May 2020 | Accepted: 28 May 2020

DOI: 10.1111/ejss.13005

SPECIAL ISSUE ARTICLE

European Journal of Soil Science WILEY

Mass-balance approach to quantify water distribution in soils based on X-ray computed tomography images

Andrey Guber[1] | **Turgut Kutlu**[2] | **Mark Rivers**[3,4] | **Alexandra Kravchenko**[1]

[1]Department of Plant, Soil and Microbial Sciences, Michigan State University, East Lansing, Michigan

[2]Soil Science Department, Bilecik Seyh Edebali University, Bilecik, Turkey

[3]Department of Geophysical Sciences and Center for Advanced Radiation Sources, The University of Chicago, Chicago, Illinois

[4]The GeoSoilEnviroCARS Facility at the Advanced Photon Source, Argonne National Laboratory, Lemont, Illinois

Correspondence
Andrey Guber, Department of Plant, Soil and Microbial Sciences, Michigan State University, East Lansing, 1066 Bogue st, MI, USA.
Email: akguber@msu.edu

Funding information
Argonne National Laboratory, Grant/Award Number: DE-AC02-06CH11357; Department of Energy—GeoSciences, Grant/Award Number: DE-FG02-94ER14466; National Science Foundation—Earth Sciences, Grant/Award Numbers: EAR−1634415, 1630399, DEB 1027253; Michigan State University; Department of Energy Great Lakes Bioenergy Research Center, Grant/Award Number: BER DE-FC02-07ER64494; National Science Foundation'; National Science Foundation'

Abstract

X-ray computed tomography (CT) is commonly used in soil science to quantify distributions of pores, water and solids within soil samples. Particularly promising for liquid visualization is dual-energy scanning of samples with added dopant solutions. The approach uses solutions of heavy elements as a proxy for the soil water and utilizes the abrupt increase of the mass attenuation coefficient of heavy elements when crossing an X-ray absorption edge, detectable by dual-energy CT scanning. However, a key step in visualization of the added liquid is image segmentation. In partially saturated soils, the X-ray CT images consist of voxels with the presence of solid, liquid and gaseous phases in different ratios. These ratios are generally ignored by the traditional image segmentation methods, which separate image voxels into groups with either zero or complete saturation by either prevailing phase. The objective of this study was to develop and test a new physically based segmentation approach that accounts for partial saturation of image voxels by liquids. We combined a theoretical equation for detected photon intensity with the mass conservation equation to compute saturation of image voxels by dopant solution applied to the soil. This approach was tested on soil micro-columns with potassium iodide (*KI*) solutions. The proposed approach outperformed the traditional segmentation methods, particularly at low and intermediate water contents. Tests conducted for *KI* solutions in the concentration ranges from 2 to 20% revealed deterioration of the method accuracy with decreasing dopant concentration in the soil. Based on the results of this study we recommend 10 wt% KI solution for quantifying spatial distribution of liquids in soils using dual-energy X-ray microtomography.

Highlights

- We developed a new approach to quantify soil water distribution based on X-ray CT.
- This approach accounts for partial saturation of image voxels by liquids.
- This approach outperforms the standard image segmentation methods.
- Its application is limited to using dual energy monochromatic X-ray beams.

KEYWORDS

image segmentation, mass-balance approach, soil X-ray CT

1 | INTRODUCTION

Dual-energy X-ray computed tomography (CT) has been used for decades to study the distribution of fluids in porous media. A γ-ray beam, used in earlier studies (Barataud, Stemmelen, & Moyne, 1996; Ferrand, Milly, & Pinder, 1986; Gardner, Campbell, & Calissendorff, 1972; Hopmans & Dane, 1986; Illangasekare, Ramsey, Jensen, & Butts, 1995; Lenhard, Dane, Parker, & Kaluarachchi, 1988; Nofziger & Swartzendruber, 1974; Oostrom, Dane, Missildine, & Lenhard, 1995; Soane, 1967), was replaced later by a synchrotron X-ray (Dicarlo, Bauters, Steenhuis, Parlange, & Bierck, 1997; McBride & Miller, 1994) with an increased intensity over tube sources and a 10^5-fold decrease in scanning time. The dual-energy technique is based on differences in mass attenuation characteristics among the soil components (i.e., minerals, organics, liquids and air), resulting in material-specific transmitted intensities (brightness) measured at different energies of the X-ray beam. The difference in the transmitted intensities at two energy levels allows for calculating volumetric contents of the soil materials in the scanned samples (Dicarlo et al., 1997; Rogasik et al., 1999). The dual-energy method was later expanded by combining the use of heavy elements (dopants or contrast agents) incorporated into the pore solution (Vinegar & Wellington, 1987; Wildenschild et al., 2002) or bound to organic matter (Peth et al., 2014; Van Loo et al., 2014), with synchrotron monochromatic beams at energy levels immediately below and above the photoelectric absorption edge of the dopant elements. Algebraic subtraction of the below-edge images from those of the above-edge visualizes the voxels with dopant presence (Agbogun, Hussein, & Al, 2013; Costanza-Robinson, Harrold, & Lieb-Lappen, 2008; Peth, 2010; Peth et al., 2014; Wildenschild et al., 2013).

Despite the significant progress in dual-energy X-ray CT over the past decade, its accuracy is still hampered by the lack of precise image segmentation techniques. Different techniques currently used for segmentation dual-energy images obtained in dopant-introduced porous medias were developed primarily for a single energy X-ray CT (Baveye et al., 2010; Iassonov, Gebrenegus, & Tuller, 2009; Sezgin & Sankur, 2004). They are based on a binary approach to image segmentation, which results in white/black images representing the objects of interest and the background. Due to the partial volume effect, the objects smaller than the scanning resolution (i.e., water and air in fine pores) are typically classified as solids. Therefore, the total visible porosity in X-ray CT images is typically much less than the directly measured soil porosity. This problem can be partially solved by image enhancement followed by multivariate classification (Glasbey & Horgan, 1995) or by multiclass segmentation (Schlüter, Sheppard, Brown, & Wildenschild, 2014). However, as Schlüter et al. (2014) pointed out: "The problem of too much unresolved porosity or too gradual intensity changes is more severe and puts the entire concept of segmentation into question".

Another drawback of the traditional segmentation methods is a lack of mass conservation. Essential volumes of water located in soil pores smaller than the scanned resolution are invisible on X-ray CT images. This impedes the progress in water flow and distribution studies at the soil pore scale. Therefore, the goal of this study was to find a physically based alternative to image segmentation in dual energy scanning applications, which would allow for estimating the volumetric content of the liquids in image voxels based on the known information about their total content in the studied soil. The specific objectives are: (a) to develop a physically based approach for quantifying saturation of image voxels by the applied dopant; (b) to test the accuracy of the approach in the absence of the partial volume effect of soil solids; (c) to compare the accuracy of the new approach with that of the traditional segmentation techniques in the presence of the partial volume effect; and (d) to evaluate the effect of dopant concentration on the accuracy of the new method.

2 | MATERIALS AND METHODS

2.1 | Theory

Detailed descriptions of the theoretical principles behind X-ray CT are provided by many sources (e.g., Als-Nielsen, 2011; Morelhão, 2016). In brief, the reconstruction of 3D X-ray CT scans produces sequences of greyscale images in which the brightness of image voxels, G_i, at the energy level, i, is linearly related to the attenuation coefficients of the materials composing these voxels and the contents of the materials within the voxels:

$$G_i = \mu_i r F, \tag{1}$$

where μ_i is the linear attenuation coefficient of the material at energy level i (cm^{-1}), r is the voxel length in the sample calculated as the pixel size of the Grasshopper camera divided by the magnification of the lens used to image the scintillator, and F is the conversion coefficient for grey values from floating point to 16-bit integer values on images (10^6).

For variably saturated soils, consisting of solid, gaseous and liquid phases, the linear attenuation coefficient can be written as (Dicarlo et al., 1997; Nofziger & Swartzendruber, 1974; Wildenschild et al., 2002):

$$\mu_i = k_i^g \rho_g S_g + k_i^s \rho_s S_s + k_i^l \rho_l S_l, \quad (2)$$

where ρ are the densities (g cm^{-3}), k_i are the mass attenuation coefficients (cm^2 g^{-1}), and S are the saturations of pore voxels (cm^3 cm^{-3}) by the gases (sub- and superscripts g), the solids (s) and the liquids (l), respectively.

When a sample is scanned at two different X-ray beam energies, the density and saturation of the individual soil phases occupying the specific voxels within the sample remain constant, whereas the mass attenuation coefficients change depending on the energy levels. For most chemical elements the mass attenuation coefficients decrease gradually with increasing energy, but for heavy elements (e.g., *Ba, Sr, I*) they increase abruptly and notably at an energy level called *K-shell edge* (Figure 1). For example, for iodine the value of k_i^I increases from 6.55 to 35.82 cm^2 g^{-1} at an energy of 33.17 KeV. This effect is commonly used to visualize spatial distribution of such elements (dopants) applied to soil as a water solution. Specifically, for the soil with applied dopant solution and scanned at the two energies, one close to but below (G_b) and the other above (G_a) the *K*-shell edge, subtraction of the two images gives:

$$\Delta G = G_a - G_b = rF\left[\left(k_a^g - k_b^g\right)\rho_g S_g + \left(k_a^s - k_b^s\right)\rho_s S_s + \left(k_a^l - k_b^l\right)\rho_l S_l\right], \quad (3)$$

where subscripts a and b denote the energy levels above or below the dopant's *K*-shell edge, respectively.

Direct implementation of Equation (3) to real soil systems is impractical in the low range of photon energy (10–50 KeV) due to the presence of a broad range of soil components, for example, minerals, with substantially different mass attenuation characteristics (Appoloni & Rios, 1994; Mudahar, Modi, & Singh, 1991; Zavel'skii, 1964). The content and spatial distribution of these components vary greatly at a microscale level, resulting in high variations in k and ρ values. However, the significant changes in mass attenuation coefficients when the energy increases from below to above the *K*-shell edge take place only for the dopants. For all other soil components, the differences in mass attenuation coefficients corresponding to the dopant-specific below- and above-*K*-shell-edge energies are very small and are commonly regarded as negligible. Thus, calculating the differences between the images below and above *K*-shell-edge energies allows visualization of locations of the dopant element.

In this study, we specifically focus on cases where a dopant is added to soil as a solution, for example potassium iodide (KI), and thus is representing the liquid phase. In such a case the terms for solids and gases in Equation (3) can be ignored, and Equation (3) can be used in a reduced form:

$$\Delta G = rF\left(k_a^l - k_b^l\right)\rho_l S_l. \quad (4)$$

The ΔG greyscale images representing spatial distribution of the dopant solution in the scanned soil samples can be obtained by an algebraic subtraction of G_b images from G_a images. It follows from Equation (4), that ΔG within an individual voxel j, ΔG_j, is linearly related to the mass content of the dopant C_d^j within the voxel:

$$\Delta G_j = rF\Delta k^d C_d^j, \quad (5)$$

where C_d^j is the mass content of the dopant in image voxels (g cm^{-3}), and $\Delta k^d = k_a^d - k_b^d$ (cm^2 g^{-1}).

Then, the sum of greyscale values across all voxels can be related to the total mass of the dopant applied to the sample M_a:

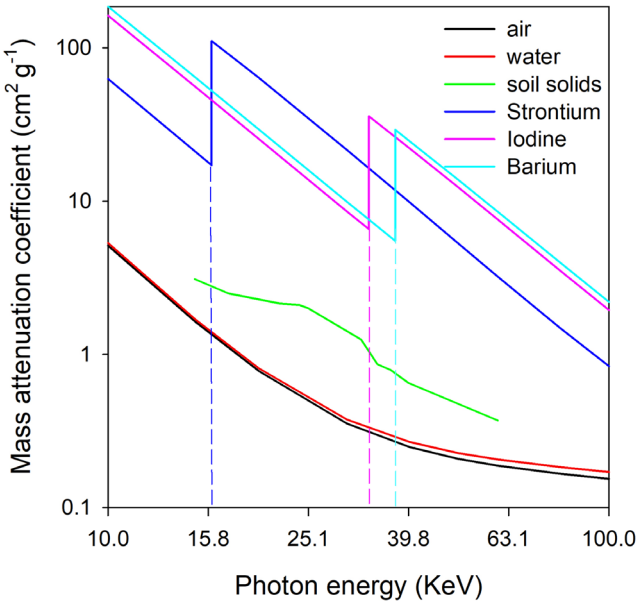

FIGURE 1 Relationships between the mass attenuation coefficients and photon energy for the selected dopants and soil components. The energy levels at K-shell edges are shown as dashed lines. Barretos soil data (soil solids) are taken from Crestana, Cesareo, and Mascarenhas (1986) [Color figure can be viewed at wileyonlinelibrary.com]

$$\sum_{j=1}^{n} \Delta G_j = rF\Delta k^d \sum_{j=1}^{n} C_d^j = rF\Delta k^d M_a / V_v, \quad (6)$$

where n is the total number of voxels containing the dopant solution in the scanned sample (−) and V_v is the voxel volume (cm^3).

Assuming that the dopant is distributed uniformly within the pore solution (i.e., it was applied to the air-dry soil and was not adsorbed on the surface of mineral or organic particles), the saturation of an individual voxel by the dopant can be calculated as:

$$S_j = C_d^j / C_d^a = \Delta G_j / rF\Delta k^d C_d^a, \quad (7)$$

where C_d^a is the concentration of the dopant in the applied solution ($g\,cm^{-3}$).

Theoretically, Equation (6) is valid for all $\Delta G_j > 0$. However, for real soils without dopant application, subtraction of G_b images from G_a images produces both positive and negative ΔG_j due to the image noise. The noise is commonly caused by counting statistics, image blur, hardware constraints or suboptimal image reconstruction (Schlüter et al., 2014). This noise is symmetrical relative to zero ΔG and overlaps with the signal (positive ΔG values) in voxels containing the dopant (Figure 2). The overlapping positive part of ΔG, caused by the presence of multiple phases (solid, liquid, gaseous and dopant) in the same voxels, introduces uncertainty into voxel classification by most image segmentation methods. This uncertainty, associated with the assumption that only a single phase is present in each individual soil voxel, causes attribution of the entire voxel to either the solid, liquid, gaseous or dopant phase by the segmentation methods. Contrary to the currently used segmentation methods, Equation (7) is free of such assumption, because the term C_d^j accounts for the partial voxel saturation by the dopant. Moreover, it allows separation of the signal (the dopant) from the noise by summing up ΔG values in voxels starting from maximum ΔG and finishing at ΔG^* (Figure 2), that is, the ΔG value at which Equation (6) holds true (i.e., the mass balance of the applied dopant is preserved in the whole images).

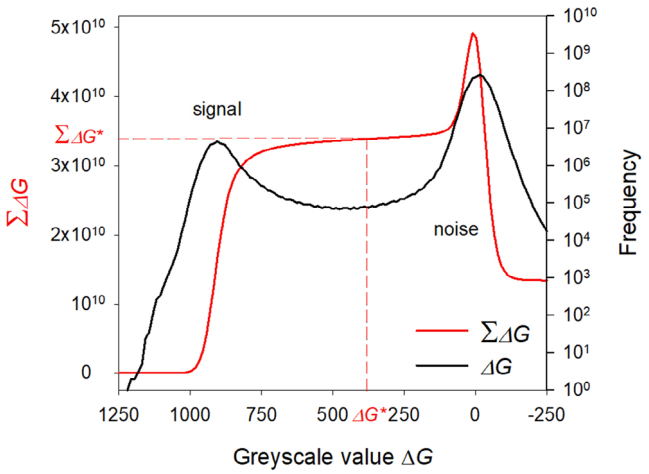

FIGURE 2 Histograms of frequency (black) and cumulative (red) distributions of greyscale values for soil after application of 10% *KI* solution. ΔG^* denotes the greyscale value on the cumulative histogram at which $\Sigma\Delta G$ corresponds to the mass of applied iodide in the soil [Color figure can be viewed at wileyonlinelibrary.com]

2.2 | Experiments

Three experiments were conducted to test the correctness of the theoretical principles described above and the accuracy of the developed mass-based approach in the soils with different pore size distributions and water contents. The *micro-tip* experiment was designed to eliminate the partial volume effect of the soil solids and air, while preserving the noise from these phases in the ΔG histograms. The dopant was applied to the *micro-tip* inserted in the dry soil, so its mass calculated using the ΔG histograms was expected to be equal to the applied mass (Equation (6)). Unlike the *micro-tip* experiment, the *micro-column* experiment was designed to evaluate the performance of the developed approach in soils with different pore-size distributions and water contents in the presence of the partial volume effect, and compare its efficiency with the traditionally used segmentation methods. In this experiment, the dopant was introduced directly to the fine, medium and coarse soil fractions at three application rates. Finally, the *concentration* experiment was performed to evaluate the effect of the dopant concentration on the accuracy of the mass-balance approach. The same volumes of the dopant but at five different concentrations were applied to the three soil aggregate fractions. Then the mass-balance approach was applied to calculate ΔG^* values and voxel saturation by the dopant. Computed ΔG^* were compared with the theoretical ΔG^* in the three soil aggregate fractions for each dopant concentration.

2.2.1 | Soil micro-columns

To test the proposed mass-balance approach for quantification of spatial distribution of soil solution, we used iodide (*I*-) as a dopant. Iodide content in natural soils is very low and typically ranges from 0.5 to 20 $mg\,kg^{-1}$ (Whitehead, 1984). High water solubility of potassium

iodide (*KI*) makes it very attractive as a dopant for dual-energy X-ray CT in porous media (Agbogun et al., 2013; Wildenschild et al., 2002, 2013).

The soil for the study was collected from the Scale-up experiment at the Marshall farm of the Great Lakes Bioenergy Research Center, Kellogg Biological Station, southwest Michigan, USA (85°24″ W, 42°24″ N). The soil was fine loamy, mixed, mesic Typic Hapludalf (Kalamazoo series) developed on a glacial outwash. The soil was collected from 0 to 10-cm depth, air-dried, mechanically crushed and sieved with an RO-TAP test sieve shaker (Model RX-29, W.S. Tyler, Mentor, OH, USA) for 1 min to obtain three soil aggregate fractions with <0.05 mm, 0.10–0.50 mm and 1.00–2.00 mm size ranges, referred to hereafter as fine, medium and coarse fractions, respectively. Soil micro-columns were prepared from these fractions for the three experiments as described below.

Micro-tip experiment

The goal of the *micro-tip* experiment was to test the validity of Equation (6). Soil micro-columns for this experiment were prepared so as to exclude the interference from the partial volume effect. For that, the dopant was separated from the soil solids. A 10-μL pipette micro-tip (Wheaton long natural polypropylene pipette micro-tip, DWK Life Sciences, Millville, NJ, USA) was filled with a 10% (0.6 M) *KI* solution and inserted into a 3-mL syringe. Then, the inner space between the syringe walls and the micro-tip was filled with air-dry soil from one of the sieved aggregate fractions (i.e., fine, medium or coarse). The inner diameter of the syringe was 8.6 mm. The inner diameter of the micro-tip ranged from 0.57 to 1.4 mm along the tip within the scanner field of view (Figure 3a).

Micro-column experiment

The goal of the *micro-column* experiment was to test the accuracy of the mass-balance approach. The dopant was added to the air-dry soil of the medium and coarse fractions in the amounts sufficient to achieve either 0.1, 0.25 or 0.4 $cm^3\ cm^{-3}$ water contents, and to the air-dry soil of the fine fraction in the amounts to achieve 0.25 or 0.4 $cm^3\ cm^{-3}$ water contents. A total of eight 3-mL syringes were used in the experiment. Each syringe was split into two sections by a plastic insert (Figure 3b). Each section contained 0.5 cm^3 of the studied soil fraction. The soil of the top sections received 10% *KI* solution in the amounts needed to achieve the studied water contents, the soil of the bottom sections remained air-dry. The top section was used to evaluate the accuracy of the method, whereas the bottom section was used as a control. The applied mass of iodide was equal to 3.82, 9.56 and 15.29 mg for the three studied water contents, respectively. In order to achieve an even distribution of the KI within the soil of the lowest water content treatment, 0.1 $cm^3\ cm^{-3}$, the iodide solution was added to the air-dry soil of medium and coarse fraction materials in a separate container. The soil was thoroughly mixed with the added solution and placed into the top sections of the micro-columns. Homogeneous mixing of water with the fine aggregate fraction was not possible; therefore, fine-fraction micro-columns with 0.1 $cm^3\ cm^{-3}$ water content were not prepared. The iodide solution of the two higher water content treatments, 0.25 and 0.4 $cm^3\ cm^{-3}$, was added to the soils of the three studied fractions from the top of the syringes with a pipette. The micro-columns were prepared 8 hr prior to the scanning to allow the solution to uniformly distribute within the soil. The syringes were plugged by syringe plungers from both the top and bottom to prevent evaporation and soil movement.

Concentration experiment

The goal of the *concentration experiment* was to evaluate the effect of the dopant concentration on the accuracy of

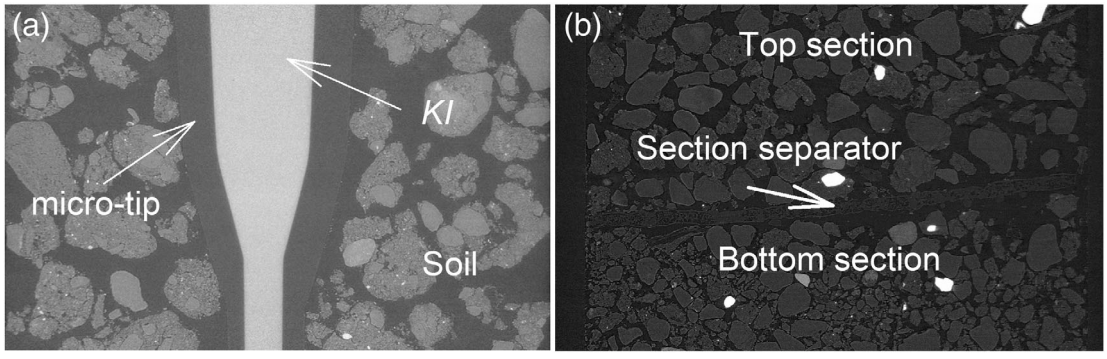

FIGURE 3 X-ray CTs of the experimental set-ups at energy level below iodine *K*-shell edge for the micro-tip (a) and micro-column (b) experiments: (a) a soil sample with a pipette micro-tip insert filled with a 10% *KI* solution; and (b) a syringe tube separated into two sections filled with the medium soil fraction. *KI* solution was applied to the top section, whereas the bottom section remained air-dry

the mass-balance approach. In this experiment, medium and coarse soil fractions were used with five *KI* concentrations: 0, 2, 5, 10 and 20% (i.e., 0, 0.12, 0.3, 0.6, 1.2 M). Potassium iodide solution was added in the amount to bring the soil to 0.30 cm^3 cm^{-3} water content. The solutions were applied 8 hr prior to scanning, similarly to the micro-column experiment.

2.2.2 | Scanning and image processing

The micro-columns were scanned at the Advanced Photon Source (APS) at the Argonne National Laboratory (GeoSoilEnviroCARS magnet beam-line 13-BM-D). We used a monochromatic X-ray beam at two energies, 33.269 and 33. 069 keV, which are above and below the iodine *K*-shell edge, respectively. We used a FLIR Grasshopper 3 CMOS camera (FLIR Systems, Inc., Wilsonville, OR, USA) with 1,920 × 1,200 pixels. Each scan collected 900 projections at 4-μm resolution, which took approximately 16 min for each energy level.

The reconstructed image sequences (1,200 slices) were processed in ImageJ/Fiji software (Schindelin et al., 2012). We first obtained ΔG_j images by subtracting the images scanned at the energy below from those above the iodine *K*-shell edge. Then we applied a non-local means denoise filter (Buades, Coll, & Morel, 2011; Darbon, Cunha, Chan, Osher, & Jensen, 2008) with the default settings (sigma = 15, smoothing factor = 1) to all ΔG_j image sequences to reduce the random noise of the greyscale values.

For the *micro-tip* experiment, we calculated the mass of the iodide in the micro-tips by the theoretical approach (Equation (6)) and by the direct counting of the voxels with *KI* solution. For the theoretical approach we used the calculated values of mass attenuation coefficients (Table 1). The direct counting of the voxels was used instead of direct measurements of iodide mass. The iodide mass in the X-ray CT-scanned portions of the micro-tips was unknown because of incomplete filling of the micro-tips by *KI* solution, for example air bubbles were visible on the images, and because of the irregular shape of the micro-tips. The total numbers of voxels were converted to the total masses of iodide in image sequences based on voxel volumes and I^- concentration in the applied solution. The relative error of I^- mass *ER* was calculated to assess the accuracy of the theoretical approach:

$$ER = (M_c - M_a)/M_a, \tag{8}$$

where M_c and M_a are calculated and the applied mass of iodide (g).

For the *micro-column* experiment, the mass of the applied iodide was known. We used ΔG_j image sequences to calculate the saturation of voxels by the *KI* solution. To simplify ImageJ/Fiji calculations Equation (7) was used in the reduced form:

$$S_j = \Delta G_j/\Delta G_t, \tag{9}$$

$$\Delta G_t = rF\Delta k^d C_d^a = 895$$

where ΔG_t is the theoretical value of ΔG for 10% *KI* solution calculated based on the mass attenuation coefficients for K^+, I^- and H_2O (Table 1).

Then the total mass of iodide was calculated in the ΔG images as:

$$\sum_{j=1}^{n} M_j^d = V_v \sum_{j=1}^{n} \Delta G_j/rF\Delta k^d, \tag{10}$$

where M_j^d is the mass of iodide in *j*-voxel (g).

The summation in Equation (10) started at $\Delta G_{\max}$ and finished at ΔG^*, where equation $\sum_{j=1}^{n} M_j^d = M_a$ held true (Figure 2). Saturation of all voxels S_j with $\Delta G_j < \Delta G^*$ was set to zero.

Equations (9) and (10) were applied to the top (with *KI* solution) and bottom (without *KI* solution) sections of the soil micro-columns (Figure 3b). The top section was used to evaluate the accuracy of the method, whereas the bottom section was used as a control.

Standard thresholding techniques available in the "Threshold" toolbox of the ImageJ/Fiji software (Table 2) were applied to the same images to compare the proposed approach with the approaches traditionally used for image segmentation. Thresholding ΔG images for the top sections of the micro-columns produced 8-bit image sequences with voxels filled with the *KI* solution. Because the standard thresholding methods did not allow us to

TABLE 1 The mass attenuation coefficients obtained by fitting equation $k = a_1 E^{a_2} + a_3 E^{a_4}$ (Manjunatha, Seenappa, Sridhar, Sowmya, & Hanumantharayappa, 2017) to the standard values of the photon mass attenuation coefficients (Hubbell & Seltzer, 2004)

Component	Molecular mass g mol^{-1}	k_a [a] cm^2 g^{-1}	k_b cm^2 g^{-1}
H_2O	18.02	0.329	0.327
K^+	39.1	2.591	2.546
I^-	126.9	35.62	6.617

[a]Subscripts a and b denote energies above (33.269 KeV) and below (33.069 KeV) the iodine *K*-shell edge.

TABLE 2 Tested thresholding methods available in the ImageJ software

#	Thresholding	Method	Reference
1	Default	Variation of the IsoData	
2	Huang	Fuzzy thresholding	Huang and Wang (1995)
3	Intermodes	Local maxima	Prewitt and Mendelsohn (1966)
4	IsoData	Averaging background and object thresholds	Ridler and Calvard (1978)
5	IJ_IsoData	Variation of the IsoData	
6	Li	Minimum cross entropy	Li and Lee (1993); Li and Tam (1998)
7	MaxEntropy	Maximum entropy	Kapur, Sahoo, and Wong (1985)
8	Mean	Mean of grey levels	Glasbey (1993)
9	MinError(I)	Fitting two Gaussian distributions	Kittler and Illingworth (1986)
10	Moments	Preserving the first three moments of the greyscale values	Tsai (1985)
11	Otsu	Minimizing the intra-class variance	Otsu (1979)
12	Percentile	Based on 50% of foreground pixels	Doyle (1962)
13	RenyiEntropy	Renyi's entropy	Kapur et al. (1985)
14	Shanbhag	Two fuzzy sets	Shanbhag (1994)
15	Triangle	A triangle algorithm	Zack, Rogers, and Latt (1977)
16	Yen	Yen's algorithm	Yen, Chang, and Chang (1995); Sezgin and Sankur (2004)

account for the partial voxel saturation, it was assumed that iodide concentration was the same in all voxels and equal to the concentration in the applied solution. The total mass of iodide in the section was computed as a product of iodide concentration in the applied solution and the total volume of voxels filled with the *KI* solution.

For the *concentration experiment*, the theoretical ΔG_t were calculated separately for each applied solution based on the mass attenuation coefficients and contents of K^+ and I^-. Then, Equation (10) was applied in the range from ΔG_{max} to ΔG^* to histograms of ΔG_j images obtained for the two soil fractions and the four concentrations of *KI* solution. The ΔG^* values obtained from the histograms were compared with the theoretical ΔG_t to assess the accuracy of the voxel saturation calculations by Equation (8).

3 | RESULTS AND DISCUSSION

3.1 | The micro-tip experiment

The ΔG histograms for the micro-tip experiment are shown in Figure 4. The histograms for soil fractions without I^- (dashed lines) have almost symmetrical shapes with ΔG of -4.0 ± 19.8, -4.8 ± 21.6 and -6.4 ± 19.9 (mean $\pm$ SD) for the fine, medium and coarse soil fractions, respectively. Theoretically, at a very small energy deviation from the *K*-shell edge, the ΔG values should be close to zero for all soil components except for I^-. The observed deviations from zero are predominantly caused by noises, which are introduced during image acquisition and subsequent

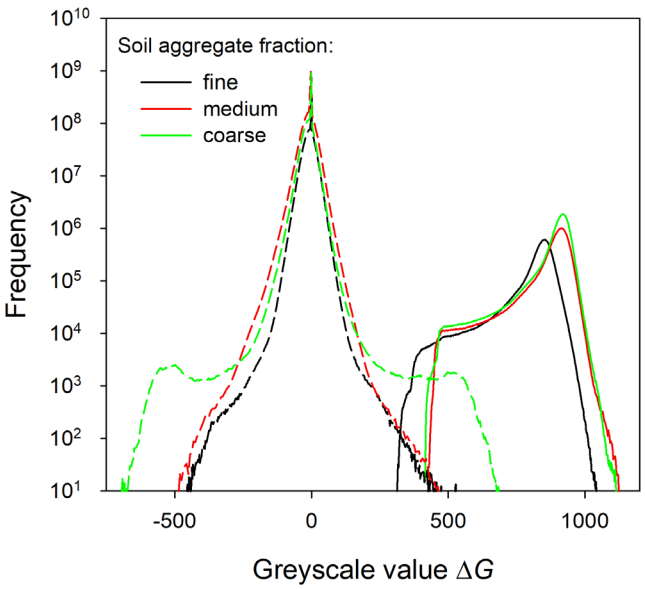

FIGURE 4 The greyscale histograms of *KI* solution (solid lines) and air-dry soil aggregate fractions (dashed lines) for the micro-tip experiment [Color figure can be viewed at wileyonlinelibrary.com]

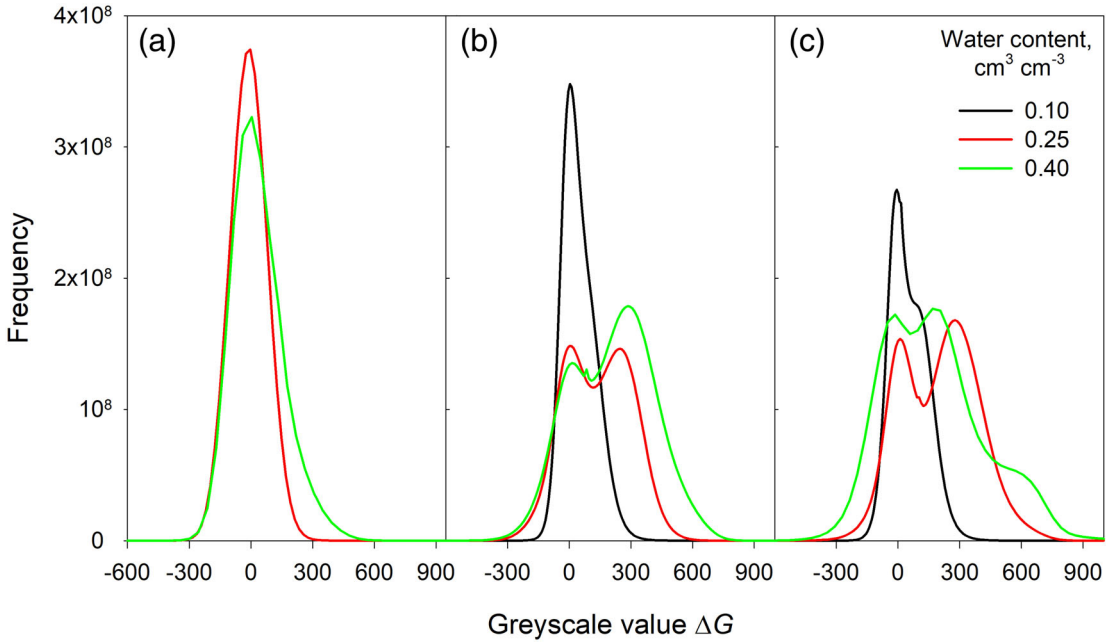

FIGURE 5 Iodide histograms for fine (a), medium (b) and coarse (c) soil aggregate fractions at the studied soil water contents [Color figure can be viewed at wileyonlinelibrary.com]

reconstruction and are only partially removed by image processing, for example by denoising filters.

Contrary to the soil histograms, the shape of *KI* histograms was asymmetrical, with clear peaks at ΔG of 853, 912 and 919 (Figure 4, solid lines) for the three studied soil aggregate fractions (i.e., fine, medium or coarse). The peaks were very close to the theoretical ΔG_t (895) calculated for the 10% *KI* solution using Equation (4), thus indicating that the implemented theoretical approach correctly estimated the iodine content. The histogram for the fine soil fraction shifted towards smaller ΔG values as compared to those for the medium and coarse fractions. The origin of this shift was not clear, but the shift led to underestimation of the mass of the applied iodide by Equation (6). Indeed, although the calculated mass errors were 0.4 and −0.8% for the medium and coarse fractions, the error was equal to 7.4% for the fine fraction. The errors were in an acceptable range considering an overall small iodide content (from 0.120 to 0.284 mg) in the micro-tips.

An important result of this experiment was the low relative number of overlapping voxels on soil and iodide histograms. The number of overlapping voxels for iodide ranged from 0.1% in the medium fraction to 2.3% in the coarse soil fraction (Figure 4). Moreover, ΔG values were rather small for the overlapping voxels, indicating that it is likely that a very small mass of iodide could be misclassified as a soil solid phase.

In summary, the results of the *micro-tip* experiment showed high accuracy in calculating total iodide mass in entirely saturated voxels, and there was only minor overlap in iodide and soil solid histograms. It remains to be seen whether the same accuracy could be achieved in voxels partly saturated by the iodide.

3.2 | The micro-column experiment

The shapes of iodide histograms differed among the three soil fractions and water contents. The iodide histograms were unimodal in the fine fraction soil at both studied water contents (Figure 5a) and in the medium and coarse fractions at 0.10 cm^3 cm^{-3} water content (Figure 5b,c). Two peaks were clearly defined in the histograms of the medium and coarse fractions at water contents of 0.25 and 0.40 cm^3 cm^{-3} (Figure 5b,c). The first peak, located at $\Delta G \approx 0$, corresponded to zero iodide content and was caused by the image noise, whereas the second peak, around $180 < \Delta G < 300$ range, corresponded to the highest iodide content. The area under the second peak and ΔG value of the peak increased with an increase in water content, as a result of increasing mass of the iodide in the soil. Interestingly, there was a third peak at water content of 0.40 cm^3 cm^{-3} in the coarse soil fraction (Figure 5c). This is likely to have reflected an association of the iodide with two pore-size groups present within the large aggregates of the coarse fraction, that is, intra- and inter-aggregate pores.

The unimodal distributions of ΔG at low water content (i.e., 0.1 cm^3 cm^{-3}) resulted in a considerable overestimation of the numbers of iodide voxels and the iodide mass by all standard thresholding methods, except the Intermodes method, for the coarse soil fraction (Figure 6a). The relative errors of iodide mass estimation (*ER*) were

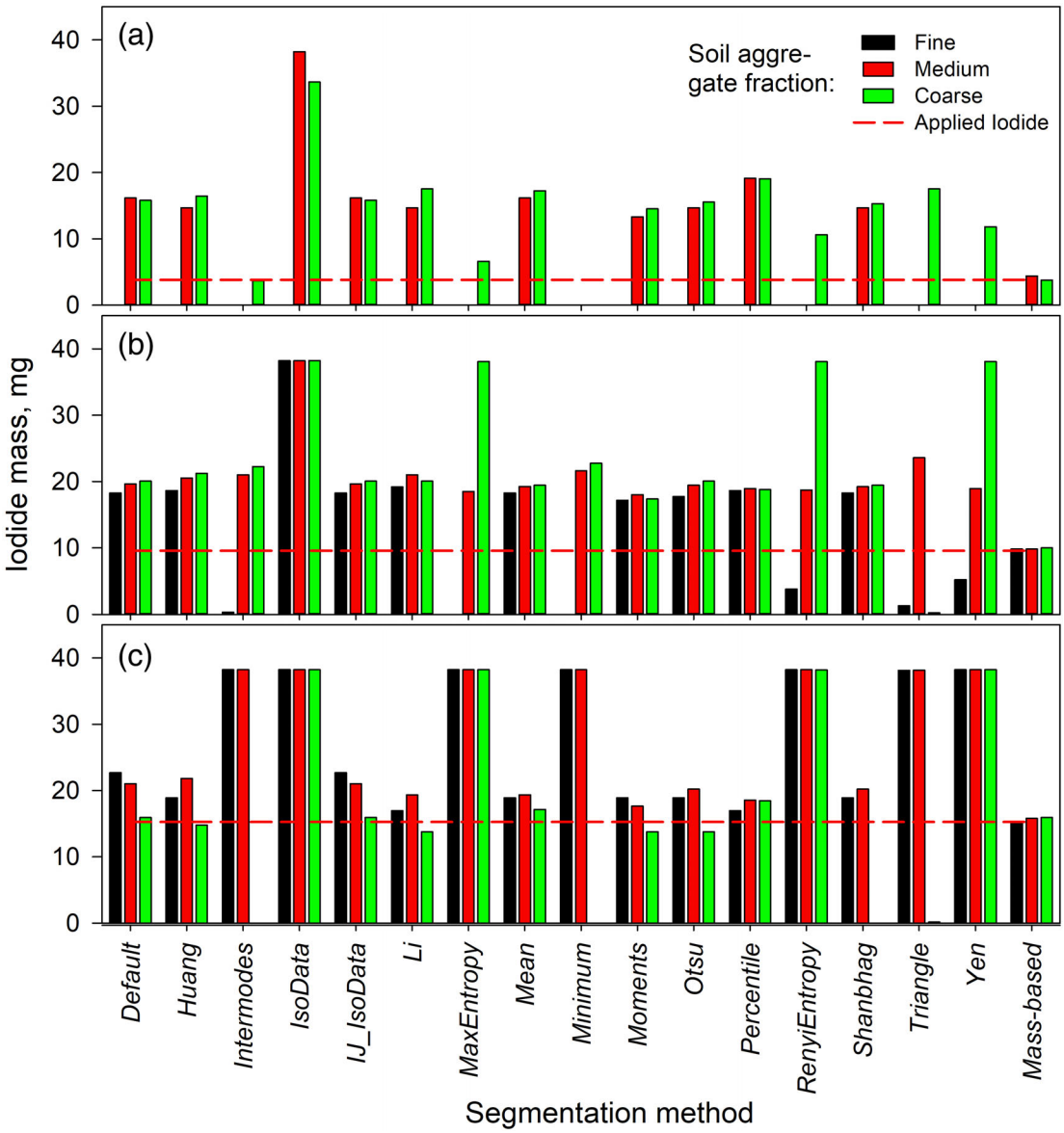

FIGURE 6 Applied (red dash line) and calculated (bars) mass of iodide for 16 standard thresholding methods and for the implemented mass-based approach at three soil water contents: 0.10 cm^3 cm^{-3} (a), 0.25 cm^3 cm^{-3} (b) and 0.40 cm^3 cm^{-3} (c) [Color figure can be viewed at wileyonlinelibrary.com]

close to 3 for most tested methods (Figure 7). The standard thresholding worked slightly better for the intermediate water content (0.25 cm^3 cm^{-3}) (Figure 6b) and reasonably well for the high water content (0.4 cm^3 cm^{-3}), particularly in the coarse soil fraction (Figure 6c), where *ER* was close to zero for 9 out of 16 methods (Figure 7). More accurate prediction of iodide mass in the coarse than in the medium fraction was likely to be associated not with the histogram shapes, which were similar in the two fractions, but with the histograms' shifts towards higher ΔG values in the coarse fraction, where the assumption of full voxel saturation by the iodide was more valid.

There was no consistency in the performance of the standard thresholding methods for the three levels of water content. The methods that performed relatively well for the low water content (e.g., Intermodes and Max Entropy) failed for the intermediate and high water contents (Figures 6 and 7).

As expected, the errors of the mass balance-based approach were close to zero for all water contents in the three soil fractions (Figure 7). Small deviations of the calculated iodide mass from that applied were caused by limited accuracy of the ImageJ/Fiji software in splitting the histograms into multiple classes. Too many ΔG classes (Bins) considerably increased the time of image processing and calculations, whereas too few Bins increased the error. In this study the parameter Bins was set to 512, the value

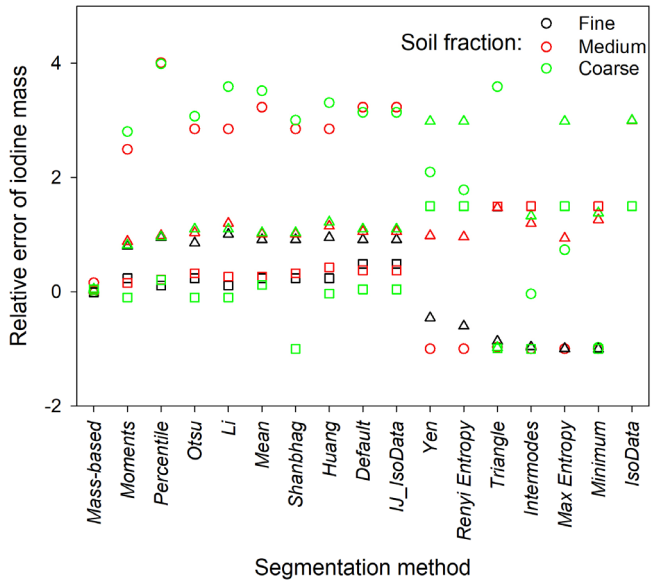

FIGURE 7 Relative errors of iodide mass for 16 thresholding methods. Symbols indicate different levels of soil water content and total applied mass of iodide: 0.10 $cm^3\ cm^{-3}$ (○), 0.25 $cm^3\ cm^{-3}$ (Δ) and 0.40 $cm^3\ cm^{-3}$ (□) iodide application [Color figure can be viewed at wileyonlinelibrary.com]

that balanced reasonably low error values with manageable computation time.

Spatial distributions of liquid within the soil samples calculated using Equation (9) and represented as voxel saturation by *KI* solution for the three soil fractions are shown in Figure 8. Visually, it appears that the solution occupies much greater area than could be expected based on soil water content levels. The reason for that is only partial saturation of voxels by the KI solution. In the fine soil fraction the majority of voxels were below 0.3 $cm^3\ cm^{-3}$ saturation (Figure 8 top line), whereas full saturation on these fine pores could be expected from a theoretical perspective. The reason for this seeming contradiction was the partial volume effect, resulting in the presence of all soil phases in each voxel. Therefore, each soil phase occupied only a fraction of voxel volume.

The partial volume effect persisted, although to a lower extent, in the medium and coarse soil fractions at all water contents. One reason for that was fine intra-aggregate porosity, for which the partial volume effect was similar to that in the fine soil fraction. Another source of the partial volume effect was thin water menisci around soil aggregates, with meniscus thickness less than the scanning resolution. As a result, the inter-aggregate voxels were partly occupied by the liquid and partly by air. The partial saturation was observed in the medium and coarse fractions at both intermediate and high water contents. Only a small number of voxels in the coarse soil were almost entirely saturated by the liquid (Figure 8 right bottom). These observations are indicative of the presence of the liquid in the studied medium and coarse soil fractions mostly in a form of menisci, consistent with the angular pore model of Tuller et al. (1999) .

Application of Equation (9) to the air-dry soil in the bottom sections of the micro-columns showed that iodide contents varied randomly from 0.34 to 56.7 μg in the 0.5-cm^3 soil columns, indicating acceptable accuracy of the theoretical method.

Despite much more accurate representation of the liquid-phase distribution in soils, the mass-based approach is still limited by the scanning resolution. It is anticipated that for pore sizes larger than the scanning resolution, that is, when only one pore or its part is present in a given image voxel, the method provides accurate estimates of the pore saturation. However, for the pores smaller than the scanning resolution it is impossible to estimate the saturation of individual pores located in the same image voxel. Therefore, the method provides only an average saturation of voxels, which, nevertheless, can be useful for studies of soil pore heterogeneity at scales ranging from a few micrometres to a few centimetres. Smaller scale (i.e., finer) resolution of the X-ray CT is limited by the exposure time, which is increasing exponentially with an increase in the resolution, whereas the larger scale (i.e., coarse) resolution is limited by the photon energy required for the beam to penetrate the sample (Wildenschild et al., 2002).

It is worth mentioning that the saturation calculated using the theoretical ΔG_t in Equation (9) may exceed 100%. This can potentially occur in voxels entirely saturated by the dopant and also affected by the image noise. It can be seen in the micro-tip histograms that there were groups of voxels with ΔG values greater than the theoretical $\Delta G_t = 895$ for the 10% *KI* solution (Figure 4). One way to resolve an oversaturation issue, while preserving the mass balance, is redistribution of the excess dopant mass among partly saturated voxels with the weights proportional to the voxel undersaturation:

$$\Delta S_k^- = S_k^- \sum \Delta S_j^+ / \sum \Delta S_k^-, \qquad (11)$$

where S_k^- is the saturation of k voxel, ΔS_j^+ is oversaturation of j voxel, and ΔS_k^- is additive to saturation of k voxel. Superscripts (−) and (+) identify under- and over-saturation of voxels, respectively. Equation (10) is valid for $\sum \Delta S_j^+ \le \sum \Delta S_k^-$; therefore, the mass excess $\sum \Delta S_j^+ - \sum \Delta S_k^-$ contributes the error of the mass-balance approach.

In summary, the developed approach provided a high-resolution distribution of the liquids in the studied soil fractions based on the physical principles of mass attenuation by heavy elements. Obtained distributions are aligned with the modern theoretical concept of water allocation in soil pores.

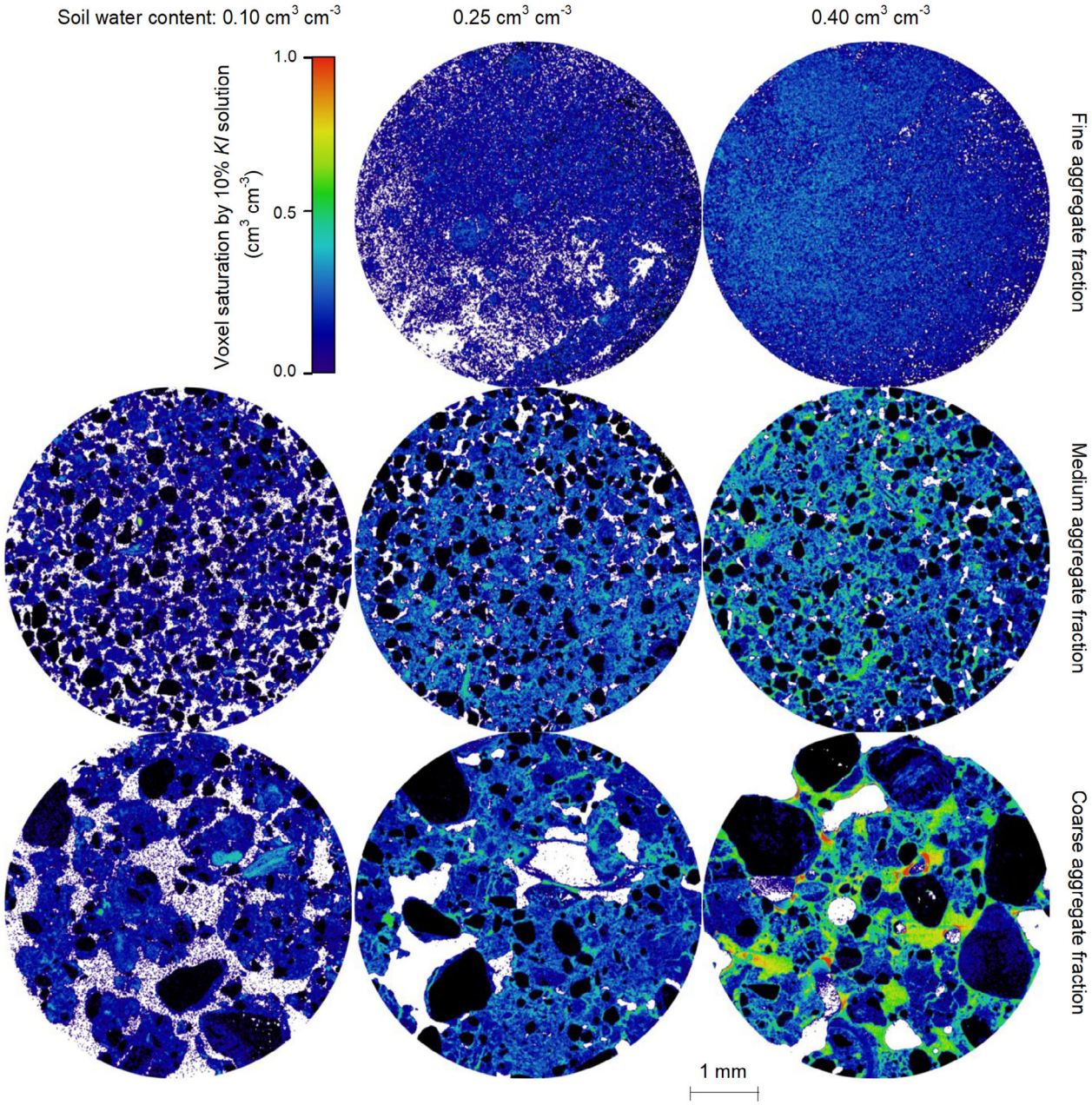

FIGURE 8 Spatial distribution of the *KI* in the three soil fractions at three soil water content levels as determined using equation (9). Colour bar indicates pore saturation by 10% KI solution; white colour shows soil volumes filled with air; black colour shows soil solids. Air and solids were segmented using adaptive-window indicator kriging (Houston, Otten, Baveye, & Hapca, 2013) after subtracting *KI* from the below *K*-shell edge images [Color figure can be viewed at wileyonlinelibrary.com]

3.3 | The effect of dopant concentration on the accuracy of the method

The shape of ΔG histograms for DI water (control) was symmetrical with a slightly negative mean value (Figure 9). The deviation from zero was likely to be caused by a general decrease in the mass attenuation coefficients with increasing energy level for all soil components (Figure 1). As *KI* concentration in the applied solution increased, the histogram means shifted toward positive ΔG values and right limbs of histograms enlarged in both medium and coarse fractions (Figure 9), indicating an overall increase in the total number of voxels with high mass attenuation coefficients.

As expected, the iodide histograms overlapped with the histograms of the image noise from the soil solids. In general, the overlapping decreased with the increasing *KI* concentration in the applied solution. However, the

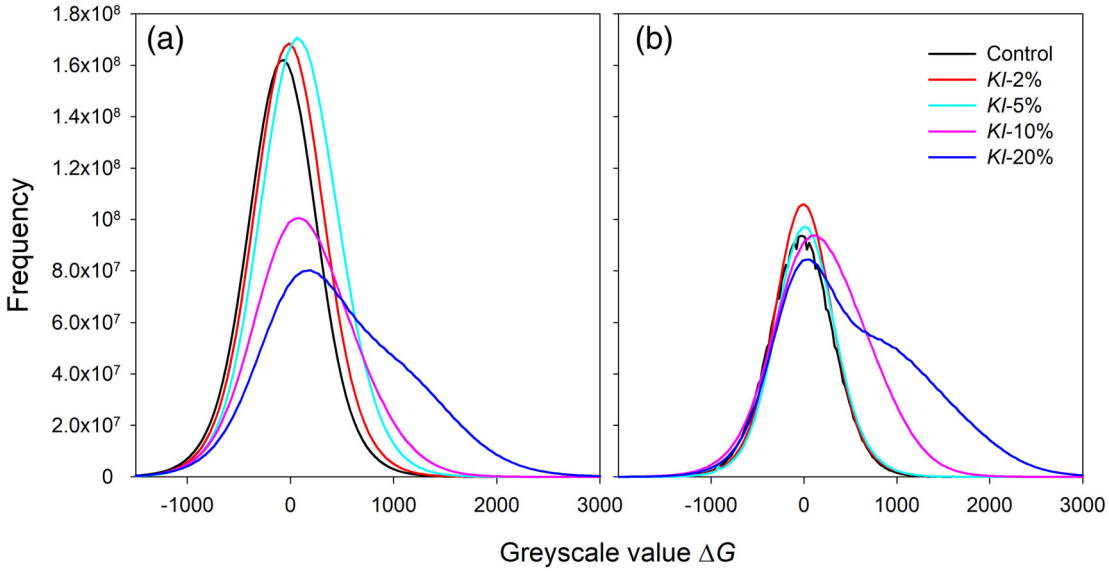

FIGURE 9 Iodide histograms in the medium (a) and coarse (b) soil fractions for five applied concentrations of *KI* [Color figure can be viewed at wileyonlinelibrary.com]

shape of most histograms remained unimodal (Figure 9), which made implementation of the standard thresholding methods impractical, as was previously demonstrated in Section 3.2. Application of the theoretical Equation (9) to the iodide histograms converged the mass balance of the applied solution in all soil samples, although at different ΔG^* values. The ΔG^* values were the smallest for the 10% KI solution, equal to 372 and 309 for the medium and coarse fractions, respectively, and the largest for the 20% KI solution, equal to 778 and 998 in the medium and coarse fractions. The ΔG^* values calculated for these concentrations were reasonable, because the theoretical ΔG_t were 895 and 1,651, respectively. However, the ΔG^* values calculated for 2 and 5% KI solutions by far exceeded the theoretical ΔG_t. As a result, saturation of individual voxels by 2 and 5% KI solutions was >100%, that contradicts to the physical sense and can be attributed solely to dominance of the image noise over signal from the dopant in those voxels.

Results of the *concentration experiment* demonstrated high sensitivity of the mass-balance approach to the dopant concentration in the applied solution. The most realistic results were obtained for 10 and 20% KI solutions. However, high concentrations can potentially affect the stability of soil structure (S. Peth, personal communication, November 25, 2019).

3.4 | Remarks on the method limitation

The mass-based approach developed to quantify spatial distribution of liquids in soil microsamples has been tested in solutions with the range of 2 to 20% KI concentrations, and it appeared to be accurate for 10 to 20% KI solutions. The method relies on the low ambient content of the dopant in the soil and uses a monochromatic photon beam with energy levels precisely adjusted to the *K*-shell edge of the dopant. It is assumed that the dopant concentration in the pore solution is the same for all image voxels, which requires a certain procedure for dopant application to soils, particularly to undisturbed soil samples. The application procedure can include, for example, soil drainage at high pressure in tempe cells (Soilmoisture Equipment Corp., Santa Barbara, CA, USA) to empty most soil pores, with subsequent gradual adding of the dopant solution to soil at low pressure levels. It takes time for the water pressure to equilibrate in the whole soil sample and stop water movement, which can introduce errors into image reconstruction. The equilibration time must be short enough to prevent an interaction between the dopant and the soil mineral and organic phases, which can result in preferential allocation of the dopant to certain image voxels, and make the assumption of a uniform dopant distribution in the pore solution invalid. This time depends on the hydraulic properties and initial soil water content and can be reduced considerably by applying suction at the bottom of the soil sample during dopant application. Note that for the ~4-μm scanning resolution and 1,920 × 1,200 pixels image size (FLIR Grasshopper 3 CMOS camera), the sample height does not exceed 5 mm, thus the equilibration time for the water contents used in this study was likely to be much shorter than 8 hr. For any particular soil and experimental condition this time can be estimated empirically or by modelling (e.g., open source software HYDRUS 1-D) (Šimůnek, Šejna, Saito, Sakai, & van Genuchten, 2009).

So far, the method has been tested on the mini-columns (0.5 cm^3 volume) filled with three soil fractions with applied 2 to 20% solutions of KI and $BaCl_2$ (results not shown). It is anticipated that the mass balance of the dopant will be preserved for a coarser scanning resolution, although with less detailed information on liquid distribution.

In summary, the implementation of the new method is limited by:

i the concentration of the dopant in the applied solution, which must preclude alteration of the soil microstructure by changing the chemical composition in the pore solution;
ii the monochromatic X-ray beam, which is less common in X-ray CT applications, as compared to the polychromatic beams used in most laboratory and medical X-ray scanners;
iii few chemical elements that do not interact with soil solids and organics and can potentially be used as dopants to quantify water distribution in soils; and
iv the size of the sample, which should be scanned within a reasonable time at two energy levels.

4 | CONCLUSIONS

A new physically based approach was developed as an alternative to the standard segmentation methods to quantify the spatial distribution of liquids in soil microcolumns. The method combines the computation of dopant mass in image voxels based on the mass attenuation coefficients, with the mass conservation equation for the dopant applied to the soil. It provides more accurate information on spatial distribution of liquids in soil as compared to the standard segmentation methods. Multiple tests of the proposed method for soil aggregate fractions of different sizes and for different soil water content levels conducted in this study showed that the new approach:

i accurately conserves the mass balance of the applied dopant;
ii accounts for partial saturation of image voxels by the liquid phase, and thus depicts more realistic spatial distributions of liquids in soil as compared to the standard segmentation methods;
iii demonstrates high sensitivity to the dopant concentration in the applied solution, with most reliable results obtained for 10 and 20% KI concentration.

ACKNOWLEDGEMENTS

Support for this research was provided in part by the USDA NIFA Program (Award # 2019-67019-29361), by the NSF LTER Program (DEB 1027253) at the Kellogg Biological Station, by USDA NC1187 project, by the Great Lakes Bioenergy Research Center, U.S. Department of Energy, Office of Science, Office of Biological and Environmental Research under Award Number DE-SC0018409, and by Michigan State University AgBioResearch. This research used resources of the Advanced Photon Source, a U.S. Department of Energy (DOE) Office of Science User Facility operated for the DOE Office of Science by Argonne National Laboratory under Contract No. DE-AC02-06CH11357. We acknowledge the support of GeoSoilEnviroCARS (Sector 13), which is supported by the National Science Foundation - Earth Sciences (EAR-1128799), and the Department of Energy, Geosciences (DE-FG02-94ER14466).

DATA AVAILABILITY STATEMENT

Data available from the corresponding author upon request

CONFLICTS OF INTEREST

The authors of the manuscript have no conflicts of interest.

ORCID

Andrey Guber https://orcid.org/0000-0002-0277-5227
Alexandra Kravchenko https://orcid.org/0000-0001-5920-927X

REFERENCES

Agbogun, H. M. D., Hussein, E. M. A., & Al, T. A. (2013). Assessment of x-ray micro-CT measurements of porosity and solute concentration distributions during diffusion in porous geologic media. *Journal of Porous Media*, *16*(8), 683–694. https://doi.org/10.1615/JPorMedia.v16.i8.10

Als-Nielsen, J., & McMorrow, D. (2011). *Elements of modern X-ray physics* (2nd ed.). Chichester, England: John Wiley & Sons Ltd. https://doi.org/10.1002/9781119998365

Appoloni, C. R., & Rios, E. A. (1994). Mass attenuation coefficients of Brazilian soils in the range 10-1450 keV. *Applied Radiation and Isotopes*, *45*, 287–291. https://doi.org/10.1016/0969-8043(94)90041-8

Barataud, F., Stemmelen, D., & Moyne, C. (1996). Identification of the hydraulic diffusivity of a soil by inverse method with dual-energy gamma ray attenuation measurements. In J. Gottlieb & P. DuChateau (Eds.), *Parameter identification and inverse problems in hydrology, geology and ecology* (pp. 123–132). Norwell, MA: Kluwer Academic Publisher.

Baveye, P. C., Laba, M., Otten, W., Bouckaert, L., Dello Sterpaio, P., Goswami, R. R., ... Sezgin, M. (2010). Observer-dependent variability of the thresholding step in the quantitative analysis of soil images and X-ray microtomography data. *Geoderma*, *157*(1–2), 51–63. https://doi.org/10.1016/j.geoderma.2010.03.015

Buades, A., Coll, B., & Morel, J.-M. (2011). Non-local means Denoising. *Image Processing on Line*, *1*, 208–212. https://doi.org/10.5201/ipol.2011.bcm

Costanza-Robinson, M. S., Harrold, K. H., & Lieb-Lappen, R. M. (2008). X-ray microtomography determination of air-water interfacial area-water saturation relationships in sandy porous media. *Environmental Science & Technology*, *42*(8), 2949–2956. https://doi.org/10.1021/es072080d

Crestana, S., Cesareo, R., & Mascarenhas, S. (1986). Using a computed tomography mini scanner in the soil science. *Soil Science*, *142*, 56–61.

Darbon, J., Cunha, A., Chan, T., Osher, S., & Jensen, G. (2008). *Fast nonlocal filtering applied to electron cryomicroscopy*. In *2008 5th IEEE International Symposium on Biomedical Imaging: From Nano to Macro, Proceedings, ISBI*. IEEE, 1331–1334. Paris, France. https://doi.org/10.1109/ISBI.2008.4541250

Dicarlo, D. A., Bauters, T. W. J., Steenhuis, T. S., Parlange, J. Y., & Bierck, B. R. (1997). High-speed measurements of three-phase flow using synchrotron X rays. *Water Resources Research*, *33*(4), 569–576. https://doi.org/10.1029/96WR03958

Doyle, W. (1962). Operation useful for similarity-invariant pattern recognition. *Journal of the Association for Computing Machinery*, *9*, 259–226.

Ferrand, L. A., Milly, P. C. D., & Pinder, G. F. (1986). Dual-gamma attenuation for the determination of porous medium saturation with respect to three fluids. *Water Resources Research*, *22*, 1657–1663.

Gardner, W. H., Campbell, G. S., & Calissendorff, C. (1972). Systematic and random errors in dual gamma energy soil bulk density and water content measurements. *Soil Science Society of America, Proceedings*, *36*, 393–398.

Glasbey, C. A. (1993). An analysis of histogram-based thresholding algorithms. *Graphical Models and Image Processing*, *55*, 532–537.

Glasbey, C. A., & Horgan, G. W. (1995). *Image analysis for the biological sciences*. Chichester, England: John Wiley & Sons.

Hopmans, J. W., & Dane, J. H. (1986). Calibration of a dual-energy gamma radiation system for multiple point measurements in a soil. *Water Resources Research*, *22*, 1109–1114.

Houston, A., Otten, W., Baveye, P., & Hapca, S. (2013). Adaptive-window indicator kriging: A thresholding method for computed tomography images of porous media. *Computational Geosciences*, *54*, 239–248. https://doi.org/10.1016/j.cageo.2012.11.016

Huang, L. K., & Wang, M. J. J. (1995). Image thresholding by minimizing the measures of fuzziness. *Pattern Recognition*, *28*, 41–51.

Hubbell, J. H., & Seltzer, S. M. (2004). Tables of X-ray mass attenuation coefficients and mass energy-absorption coefficients from 1 keV to 20 MeV for elements Z=1 to 92 and 48 additional substances of Dosimetric interest. X-ray mass attenuation coefficients. *NIST Standard Reference Database*, *126*. https://dx.doi.org/10.18434/T4D01F. https://physics.nist.gov/PhysRefData/XrayMassCoef/tab3.html. Accessed from 15/6/2020

Iassonov, P., Gebrenegus, T., & Tuller, M. (2009). Segmentation of X-ray CT images of porous materials: A crucial step for characterization and quantitative analysis of pore structures. *Water Resources Research*, *45*, W09415. https://doi.org/10.1029/2009WR008087

Illangasekare, T. H., Ramsey, J. L. J., Jensen, K. H., & Butts, M. B. (1995). Experimental study of movement and distribution of dense organic contaminants in heterogeneous aquifers. *Journal of Contaminant Hydrology*, *20*, 1–25.

Kapur, J. N., Sahoo, P. K., & Wong, A. K. C. (1985). A new method for gray-level picture thresholding using the entropy of the histogram. *Graphical Models and Image Processing*, *29*, 273–285.

Kittler, J., & Illingworth, J. (1986). Minimum error thresholding. *Pattern Recognition*, *19*, 41–47.

Lenhard, R. J., Dane, J. H., Parker, J. C., & Kaluarachchi, J. J. (1988). Measurement and simulation of one-dimensional transient three-phase flow for monotonic drainage paths. *Water Resources Research*, *24*, 853–863.

Li, C. H., & Lee, C. K. (1993). Minimum cross-entropy thresholding. *Pattern Recognition*, *26*, 617–625.

Li, C. H., & Tam, P. K. S. (1998). An iterative algorithm for minimum cross-entropy thresholding. *Pattern Recognition Letters*, *19*, 771–776.

Manjunatha, H. C., Seenappa, L., Sridhar, K. N., Sowmya, N., & Hanumantharayappa, C. (2017). Empirical formulae for mass attenuation and energy absorption coefficients from 1 keV to 20 MeV. *European Physical Journal D: Atomic, Molecular, Optical and Plasma Physics*, *71*, 235. https://doi.org/10.1140/epjd/e2017-70679-7

McBride, J. F. & Miller, C. T. (1994). Measurement of phase fractions in porous media by using x rays. Res. Rep. ER/1.94. Center for Multiphase Res., Dep. of Environ. Sci. and Eng., University of North Carolina, Chapel Hill, NC.

Morelhão, S. L. (2016). Fundamentals of X-ray physics. In *Computer simulation tools for X-ray analysis Graduate Texts in Physics* (pp. 1–57). Cham, Switzerland: Springer. https://doi.org/10.1007/978-3-319-19554-4_1

Mudahar, G. S., Modi, S., & Singh, M. (1991). Total and partial mass attenuation coefficients of soil as a function of chemical composition. *Applied Radiation and Isotopes*, *42*, 13–18.

Nofziger, D. L., & Swartzendruber, D. (1974). Material content of binary mixtures as measured with a dual-energy beam of gamma rays. *Journal of Applied Physics*, *45*, 5443–5449.

Oostrom, M., Dane, J. H., Missildine, B. C., & Lenhard, R. J. (1995). Error analysis of dual-energy gamma radiation measurements. *Soil Science*, *160*, 28–42.

Or, D., & Tuller, M. (1999). Liquid retention and interfacial area in variably saturated porous media: Upscaling from single-pore to sample-scale model. *Water Resources Research*, *35*(12), 3591–3605.

Otsu, N. (1979). A threshold selection method from gray level histograms. *IEEE Transactions on Systems, Man, and Cybernetics*, *9*, 62–66.

Peth, S. (2010). Applications of microtomography in soils and sediments. In B. Singh & M. Gräfe (Eds.), *Synchrotron-based techniques in soil and sediments Developments in Soil Science* (Vol. 34, pp. 73–101). Amsterdam, The Netherlands: Elsevier B.V.

Peth, S., Chenu, C., Leblond, N., Mordhorst, A., Garnier, P., Nunan, N., ... Beckmann, F. (2014). Localization of soil organic matter in soil aggregates using synchrotron-based X-ray microtomography. *Soil Biology & Biochemistry*, *78*, 189–194. https://doi.org/10.1016/j.soilbio.2014.07.024

Prewitt, J. M. S., & Mendelsohn, M. L. (1966). The analysis of cell images. *Annals of the New York Academy of Sciences*, *128*, 1035–1053.

Ridler, T. W., & Calvard, S. (1978). Picture thresholding using an iterative selection method. *IEEE Transactions on Systems, Man, and Cybernetics*, *8*, 630–632.

Rogasik, H., Crawford, J., Wendroth, O., Young, I., Joschko, M., & Ritz, K. (1999). Discrimination of soil phases by dual energy X-ray tomography. *Soil Science Society of America Journal*, *63*, 741–751.

Schindelin, J., Arganda-Carreras, I., Frise, E., Kaynig, V., Longair, M., Pietzsch, T., ... Cardona, A. (2012). Fiji: An open-source platform for biological-image analysis. *Nature Methods*, *97*, 676–682. https://doi.org/10.1038/nmeth.2019

Schlüter, S., Sheppard, A., Brown, K., & Wildenschild, D. (2014). Image processing of multiphase images obtained via X-ray microtomography: A review. *Water Resources Research*, *50*, 3615–3639. https://doi.org/10.1002/2014WR015256

Sezgin, M., & Sankur, B. (2004). Survey over image thresholding techniques and quantitative performance evaluation. *Journal of Electronic Imaging*, *13*(1), 146–165.

Shanbhag, A. G. (1994). Utilization of information measure as a means of image thresholding. *Graphical Models and Image Processing*, *56*(5), 414–419.

Šimůnek, J. Šejna, M., Saito, H., Sakai, M. & van Genuchten, M.Th. 2009. The HYDRUS-1D software package for simulating the one-dimensional movement of water, heat, and multiple solutes in variably-saturated media, version 4.08. Department of Environmental Sciences, University of California, Riverside, CA.

Soane, B. D. (1967). Dual energy gamma-ray transmission for coincident measurement of water content and dry bulk density of soil. *Nature*, *214*(5094), 1273–1274. https://doi.org/10.1038/2141273a0

Tsai, W. H. (1985). Moment-preserving thresholding: A new approach. *Graphical Models and Image Processing*, *19*, 377–393.

Tuller, M., Or, D., & Dudley, L. M. (1999). Adsorption and capillary condensation in porous media: Liquid retention and interfacial configurations in angular pores. *Water Resources Research*, *35* (7), 1949–1964.

Van Loo, D., Bouckaert, L., Leroux, O., Pauwels, E., Dierick, M., Van Hoorebeke, L., ... Sleutel, S. (2014). Contrast agents for soil investigation with X-ray computed tomography. *Geoderma*, *213*, 485–491. https://doi.org/10.1016/j.geoderma.2013.08.036

Vinegar, H. J., & Wellington, S. L. (1987). Tomographic imaging of three-phase flow experiments. *The Review of Scientific Instruments*, *58*(1), 96–107.

Whitehead, D. C. (1984). The distribution and transformations of iodine in the environment. *Environment International*, *10*, 321–339.

Wildenschild, D., Hopmans, J. W., Vaz, C. M. P., Rivers, M. L., Rikard, D., & Christensen, B. S. B. (2002). Using X-ray computed tomography in hydrology: Systems, resolutions, and limitations. *Journal of Hydrology*, *267*, 285–297.

Wildenschild, D., Rivers, M. L., Porter, M. L., Iltis, G. C., Armstrong, R. T., & Davit, Y. (2013). Using synchrotron-based X-ray microtomography and functional contrast agents in environmental applications. In S. H. Anderson & J. W. Hopmans (Eds.), *Soil–water–root processes: Advances in tomography and imaging* (pp. 1–22). Madison, WI: The Soil Science Society of America, Inc..

Yen, J. C., Chang, F. J., & Chang, S. (1995). A new criterion for automatic multilevel thresholding. *IEEE Transactions on Image Processing*, *4*, 370–378.

Zack, G. W., Rogers, W. E., & Latt, S. A. (1977). Automatic measurement of sister chromatid exchange frequency. *The Journal of Histochemistry and Cytochemistry*, *25*(7), 741–753.

Zavel'skii, F. S. (1964). Mass absorption coefficients of *y*-radiation in soils and errors in measurements made by the *y* method. *Atomic Energy*, *16*, 266.

How to cite this article: Guber A, Kutlu T, Rivers M, Kravchenko A. Mass-balance approach to quantify water distribution in soils based on X-ray computed tomography images. *Eur J Soil Sci*. 2021;72:578–592. https://doi.org/10.1111/ejss.13005